

Collective intercellular communication through ultra-fast hydrodynamic trigger waves

Arnold J. T. M. Mathijssen¹, Joshua Culver², M. Saad Bhamla^{2*} & Manu Prakash^{1*}

The biophysical relationships between sensors and actuators^{1–5} have been fundamental to the development of complex life forms. Swimming organisms generate abundant flows that persist in aquatic environments^{6–13}, and responding promptly to external stimuli is key to survival^{14–19}. Here we present the discovery of ‘hydrodynamic trigger waves’ in cellular communities of the protist *Spirostomum ambiguum* that propagate—in a manner similar to a chain reaction^{20–22}—hundreds of times faster than their swimming speed. By coiling its cytoskeleton, *Spirostomum* can contract its long body by 60% within milliseconds²³, experiencing accelerations that can reach forces of 14g. We show that a single cellular contraction (the transmitter) generates long-ranged vortex flows at intermediate Reynolds numbers that can, in turn, trigger neighbouring cells (the receivers). To measure the sensitivity to hydrodynamic signals in these receiver cells, we present a high-throughput suction–flow device for probing mechanosensitive ion channels²⁴ by back-calculating the microscopic forces on the cell membrane. We analyse and quantitatively model the ultra-fast hydrodynamic trigger waves in a universal framework of antenna and percolation theory^{25,26}, and reveal a phase transition that requires a critical colony density to sustain collective communication. Our results suggest that this signalling could help to organize cohabiting communities over large distances and influence long-term behaviour through gene expression (comparable to quorum sensing¹⁶). In more immediate terms, because contractions release toxins²⁷, synchronized discharges could facilitate the repulsion of large predators or immobilize large prey. We postulate that numerous aquatic organisms other than protists could coordinate their behaviour using variations of hydrodynamic trigger waves.

For reliable communication over large distances, biological signals must be resilient to noise in complex environments. A robust solution is provided by trigger waves—biochemical wave fronts that are passed on from one reactant to the next, sustaining both signal speed and amplitude^{20–22}. Key examples are neuronal action potentials, which travel at around 100 metres per second, mitotic waves in *Xenopus* eggs, and Ca²⁺ waves in numerous tissues²². Trigger waves are very fast and specific, but suffer from a disadvantage in that they require an excitable medium (a cellular membrane or the cytoplasm) or close physical contact (in the case of neurons), such that the signal stops if the connection is cut.

Another solution is to advect information by flows; this facilitates the endocrine system (adrenaline release at 30 mm s⁻¹)²² and cytoplasmic streaming²⁸. More generally, long-range hydrodynamic interactions mediate collective motion in ‘living fluids’, which include swarms of bacteria, many aquatic and marine animals as well as micro-robots^{6–13}. As such, hydrodynamic signals can bridge large distances between cells or organisms but are generally slower, decay with distance or time, and fundamentally lack midway signal reinforcement.

Here we report the discovery of hydrodynamic trigger waves, which represent a hybrid mechanism that combines incessant propagation and high speeds (around 0.25 m s⁻¹) with long-range connectivity between freely swimming cells.

S. ambiguum is one of the largest unicellular protozoans, with a body length (L_0) of 1.1 ± 0.2 mm (Fig. 1a, b). By coordinating its cilia in metachronal waves (Supplementary Videos 1, 2), *S. ambiguum* swims at low Reynolds numbers (Re_0); that is, $Re_0 = \frac{L_0 V_0}{\nu} \approx 0.2$, in which the swimming speed (V_0) is about 0.2 mm s^{-1} in fresh water of kinematic viscosity (ν) of $1 \text{ mm}^2 \text{ s}^{-1}$ and density (ρ) of 1 g ml^{-1} . However, the cell can rapidly contract to a fraction (f_c) of 0.40 ± 0.03 of its total length as a defence against predators, with a time of contraction (τ_c) of 4.64 ± 0.15 ms (Fig. 1a, c, Supplementary Video 3). Then, the contracting cell releases toxins²⁷ as the transient Reynolds number (Re_T) surges, reaching levels of $Re_T = \frac{(1-f_c)L_0^2}{2\nu\tau_c} \approx 50$. After contraction, the cell slowly relaxes (with a relaxation time (τ_r) of about 1 s) as homeostasis is restored. The underlying biochemical mechanisms are summarized in Fig. 1d.

To quantify these dynamics systematically, we develop an electrical stimulation apparatus²³ that has microsecond precision, synchronized with high-speed (10,000 frames per second) microscopy (Supplementary Information, section 2). Figure 1e shows the cell length, velocity and acceleration; using the statistics of thousands of cells, we construct the complete phase diagram of contractile behaviour (Extended Data Fig. 1). The velocity peaks (V_{\max}) at $0.22 \pm 0.01 \text{ m s}^{-1}$ and the acceleration peaks (A_{\max}) at $139 \pm 28 \text{ m s}^{-2}$, approximately equal to forces of 14g. Unlike other rapid cellular movements (such as nematocyst firing²⁹), *Spirostomum* is capable of repeating this actuation over and over again, which makes it a useful model organism for studying ultra-fast motion in biology⁴.

The contraction of the cell generates long-ranged flows around the organism, which we analyse in a liquid film experiment (Fig. 2a). The measured flow structure is contractile along the major axis of the cell (Fig. 2c, d, Supplementary Video 4), and resembles the ‘puller-type stresslet’ that is often produced by microorganisms^{7,10,13}. However, a marked difference between these stresslets and the flow structure that we measure is that, in the latter, vortices emerge that expand into the medium over time. This vortex generation is a signature of inertia, which is also apparent as a delay in fluid motion (Fig. 2e)—the boundary-layer width (δ) grows as $\delta \propto \sqrt{\nu t}$ (in which t denotes time)¹⁵. Conducting control experiments by suspending *Spirostomum* in high-viscosity medium shows no such delay and no vortices, consistent with the Stokesian stresslet ($\nu = 50 \text{ mm}^2 \text{ s}^{-1}$ and $\tau_c = 15$ ms, so $Re_T \approx 0.3$).

To model the inertial flow in the liquid film, we therefore solve the linearized Navier–Stokes (LNS) equations¹² using the method of images¹³ (Fig. 2b). We model the contraction with ten equal and opposite point forces ($f_k(t')$), distributed along the cell at positions $r_k(t')$, with $|m| \leq 100$ image reflections. This yields the flow:

$$v_c(\mathbf{r}, t) = \sum_{k,m} \int_0^t \mathcal{Q}(\mathbf{r} - \mathbf{r}_k - m\mathbf{H}\mathbf{e}_z, t - t') \cdot f_k(t') dt' \quad (1)$$

in which $\mathcal{Q}(\mathbf{r}, t)$ is the Green’s function tensor with inertial memory kernel (Supplementary Information, section 3a–c). Importantly, both

¹Department of Bioengineering, Stanford University, Stanford, CA, USA. ²School of Chemical & Biomolecular Engineering, Georgia Institute of Technology, Atlanta, GA, USA. *e-mail: saadb@chbe.gatech.edu; manup@stanford.edu

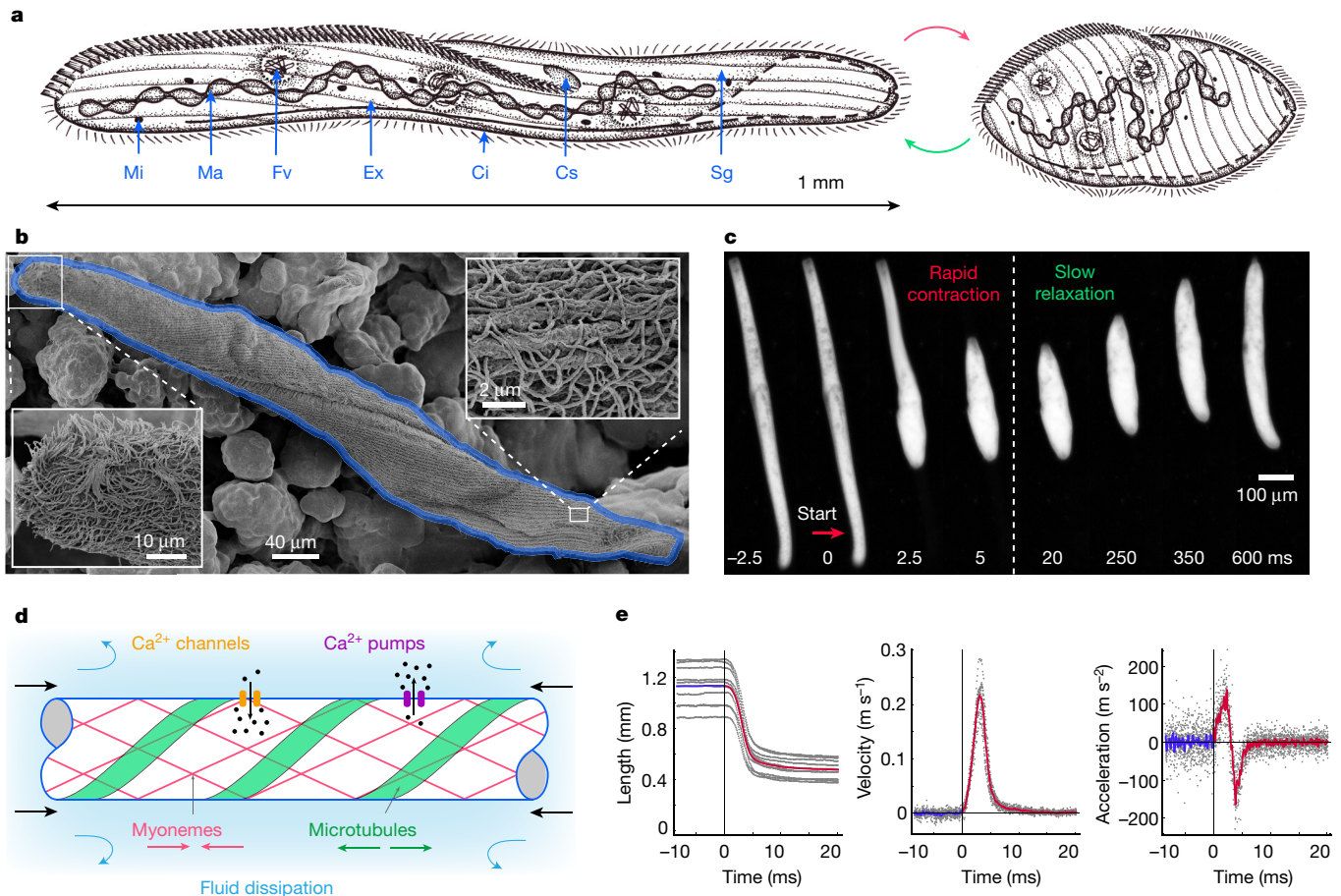


Fig. 1 | Contraction dynamics of *Spirostomum*. **a**, Diagram of the anatomy of *S. ambiguum*. Ci, cilia; cs, cytostome; ex, extrusomes containing toxins; fv, food vacuoles; mi, micronuclei; ma, macronuclear nodules; sg, somatic grooves. **b**, Scanning electron microscopy image. Insets highlight cilia and somatic grooves. $n = 21$ independent repeated experiments, using different organisms and giving similar results. **c**, Collage of a spontaneous contraction and recovery, without electric stimulation. $n = 48$ experiments. **d**, Biochemistry diagram of antagonistic contraction and relaxation mechanisms (Supplementary Information, section 2a). At rest, the cell maintains a low internal Ca^{2+} concentration

using ion pumps (purple). When triggered, ion channels (orange) open to rapidly raise the Ca^{2+} concentration. These ions bind to ‘myoneme’ filaments (red) that generate tensile forces. The rapid acceleration is halted by the cytoskeleton (green) and fluid dissipation (blue). To recover, the ion pumps reduce the Ca^{2+} concentration, so that the myonemes relax and the elastic microtubules slowly restore elongation. **e**, Kinematics of organism length L , velocity $1/2\partial_t L$ and acceleration $1/2\partial_t^2 L$. Average values (red) for ten different organisms (grey) triggered by electric stimulation ($|E| = 1.5 \text{ kV m}^{-1}$, with contraction onsets aligned at $t = 0$) are shown. $n = 216$ experiments, at 8 different pulse strengths.

the spatial and temporal elements of this model agree with the measurements (Supplementary Information, section 3d); particularly the flow structure and magnitude (Fig. 2c, Extended Data Figs. 2–5), the vortex dispersion (Supplementary Video 5) and the time-integrated tracer dynamics (Fig. 2d).

Next, the effect of inertial mixing is highlighted by simulating tracer particles during the contraction of the organism, followed by a slow relaxation (Fig. 2f, Supplementary Information, section 3e). Traditionally, the scallop theorem forbids mixing by any reciprocal motion in viscous fluids⁶, which affects many microbiological and industrial applications^{3,7–11}. However, we find that *Spirostomum* can use inertia to displace particles up to 10% of its body length per individual contraction–relaxation. This effect could further facilitate the dispersal of toxins and enhance food transport³, substantially outcompeting thermal diffusion with Péclet numbers $\text{Pe} = \frac{LV}{D} \gg 1$ (in which D is the diffusion coefficient) for even the smallest molecules.

To detect predators, organisms must sense surrounding flows^{5,14–19}. The strain rate of the moving liquid ($\dot{\gamma}$) exerts hydrodynamic stresses (S) of approximately $\rho \times \nu \times \dot{\gamma}$, which leads to an increased tension (T) of about $S \times L$. This stretches the cell membrane, such that its mechanosensitive ion channels are pulled open—which ultimately triggers the contraction^{18,24}.

To probe this rheosensitivity, we develop a high-throughput (about ten cells per second) microfluidic assay (Fig. 3a, Extended Data Fig. 6).

In this radially symmetric device, we introduce liquid with organisms on the outer edge and draw the liquid into a central sink, which emulates suction into the mouth of a predator. As cells are pulled towards the sink, the strain rate $\dot{\gamma} \propto 1/\rho^2$ of the liquid increases with decreasing distance ρ (Supplementary Information, section 4a) until they reach a threshold for contraction ($\dot{\gamma}_c$) (Supplementary Video 6). This geometry was inspired by ‘spaghettication’³⁰, a stretching induced by tidal forces near a black hole that is rendered here on a microscopic scale (Supplementary Information, section 4b). Imaged from below, we observe that all cells are triggered around a ring of radius ρ_c , the ‘event horizon’ (Fig. 3b). We therefore obtain the critical strain rate, $\dot{\gamma}_c = 88 \pm 3 \text{ s}^{-1}$. We then map this measurement to a more-intrinsic property—the critical tension required for ion channel gating (T_c), which does not depend on cell geometry. Crucially, one can use this macroscopic flow to back-calculate the microscopic forces. We use the method of regularized Stokeslets³¹ to compute—for each organism—the force distribution on the membrane immediately before the contraction (Fig. 3c, Supplementary Information, section 4c). Integrating this force yields the critical tension $T_c = 0.17 \pm 0.02 \text{ mN m}^{-1}$ (Fig. 3d). This technique can be applied straightforwardly to other organisms with different sizes or more-complex shapes.

These measurements are consolidated with established theoretical results for ion channel gating²⁴. Using the ‘two-state model’, the probability for a channel to open ($P_o(T)$) is estimated as a function of applied

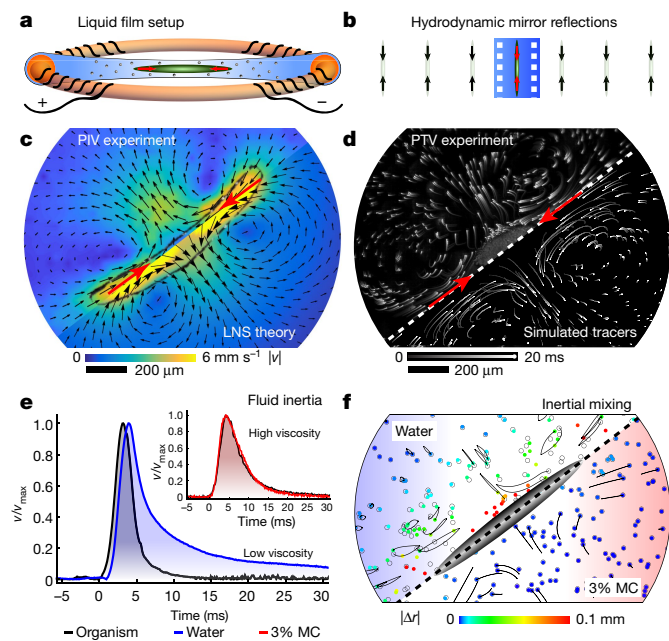


Fig. 2 | Flow generation during contractions. **a**, Diagram of experimental setup. A liquid film is suspended in a ring, with two electrodes. **b**, Diagram of hydrodynamic image systems reflected by water–air interfaces. **c**, Comparison of particle image velocimetry (PIV) measurements (top left) and LNS theory (bottom right) (see equation (1)), separated by a white dashed line (symmetry axis). In both cases, the flow is averaged over 40 ms, after the onset of contraction (Extended Data Figs. 2, 4, Supplementary Information, section 3d). $n = 46$ experiments. **d**, Comparison of experimental (top left) and simulated (bottom right) tracer dynamics, for 20 ms after the onset of contraction, separated by a white dashed line. **e**, Fluid inertia induces an offset between the organism velocity (black, defined as $\partial_t L$) and flow velocity (defined as the average over a tracer ensemble; Supplementary Information, section 3a) at low viscosity (water, $\nu = 1 \text{ mm}^2 \text{ s}^{-1}$; blue). Extended Data Figure 5 gives the theoretical result. Inset shows control at high viscosity (3% methyl cellulose (MC), $\nu = 50 \text{ mm}^2 \text{ s}^{-1}$; red). $n = 17$ experiments. **f**, Displacement of tracer particles (Δr) after an individual contraction and relaxation, simulated for low (blue) and high (red) viscosities. Open circles are the initial positions, coloured points are the final positions and a few trajectories are shown in black.

tension (Supplementary Information, section 4d). This probability transitions at a threshold tension of $T_c^{\text{theory}} \approx 0.20 \text{ mN m}^{-1}$, which is in good agreement with the experiments. More-refined future models should also include cooperative gating effects but this two-state model already provides physical insights. Specifically, our model underlines the importance of the spatial distribution of hydrodynamic stresses, and enables one to predict the stimulation threshold for other organisms or geometries.

In particular, the cell size has a major role in the rheosensitivity of the cell. The observed γ_c decreases significantly with length (Fig. 3e) such that larger cells require smaller stimuli to contract, which is also predicted theoretically (Supplementary Information, section 4e, f). This suggests that longer organisms are better sensors, which is probably an evolutionary advantage in discerning predators; this could help to elucidate why *Spirostomum* is one of the longest known ciliates, and why it takes an unusual cigar shape. Moreover, cell contraction also reduces the surface-to-volume ratio, which may act as an adaptive feedback mechanism to tune the sensitivity of the cell.

To ascertain the physiological role of contractile behaviour, we observe *Spirostomum* in undisturbed growth chambers over long periods of time. The cells tend to self-assemble into clusters, as is reproduced by mixing cultures and then recording accumulation with time-lapse imaging (Supplementary Information, section 5a, Supplementary Video 7). Once close together, the organisms exhibit

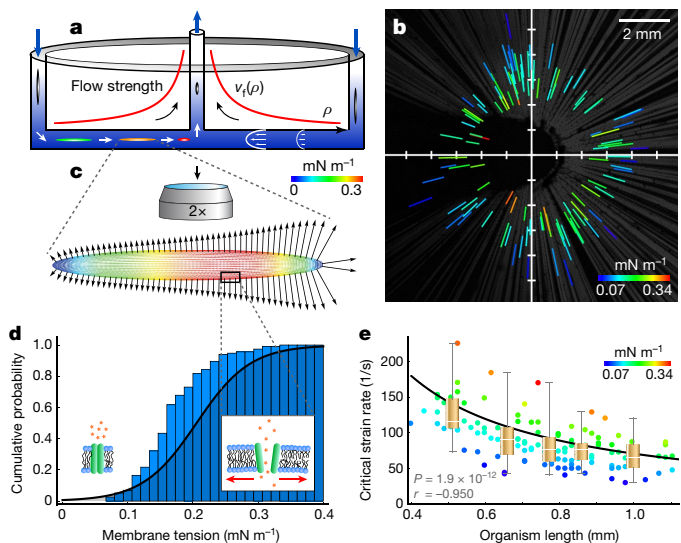


Fig. 3 | Rheosensing experiments. **a**, Diagram of microfluidic set-up. The red curve shows flow strength versus radial distance. **b**, Grey lines are organism trajectories, generated as the organisms move towards the central outlet (which is located at the origin). Coloured lines show maximum membrane tension and position at the onset of contraction. One experiment with $n = 115$ organisms is shown, out of $n = 17$ experiments. **c**, Hydrodynamic forces (arrows) and membrane tension (colours), calculated using the method of regularized Stokeslets. **d**, Cumulative distribution function (cumulative histogram) (CDF(T_c)) of the measured critical membrane tension (blue) ($n = 115$ organisms) compared to the theoretical gating probability ($P_o(T_c)$) of a mechanosensitive ion channel (black line) (Supplementary Information, section 4e). **e**, Critical strain rate versus organism length ($\gamma_c(L)$). Points are individual measurements, and colours indicate the corresponding membrane tension. Box and whisker plots are shown for 5 subgroups of $n = 23$ organisms. Box edges show the 25% and 75% quantiles, and the middle line is the median. Whiskers show the furthest outliers. The anti-correlation is statistically quantified with the Pearson correlation coefficient r and the P value (Supplementary Information, section 4f). The black line is the theoretical prediction using the method of regularized Stokeslets.

a collective phenomenon: when a first cell spontaneously contracts, it generates a flow that can trigger its neighbours to contract—and hence initiate a cascade of contractions that propagates through the colony (Fig. 4a, Extended Data Fig. 7, Supplementary Information, section 5, Supplementary Video 8). These hydrodynamic trigger waves travel at speeds (v_w) of about 0.25 m s^{-1} (Fig. 4b), which are not inappreciable compared to human neurotransmission²².

We examine the communication potential by first considering pairwise interactions (Fig. 4c, Supplementary Information, section 5c). When organism A (blue) transmits a signal (following equation (1)), organism B (purple) responds if it crosses the red line (γ_c). This model agrees with experiments for different configurations (ρ, θ and ϕ) (Fig. 4d, e, Extended Data Fig. 8), which shows that not only the distance but also relative orientations matter in propagating the trigger wave. Specifically, ‘one-way streets’ can form, along which a signal can only travel from A to B—for example, configuration $(\rho, \frac{\pi}{2}, \frac{\pi}{2})$ versus $(\rho, 0, \frac{\pi}{2})$ —as the flow is inherently directional. We quantify this using antenna theory (Supplementary Information, section 5d), which was originally designed for electromagnetic radiators, and show that the hydrodynamic signals are approximately two times stronger along the body axis (directive gain 2.79 dB).

Using these building blocks, we consider interactions between many organisms by simulating large colonies with different cell densities (N) (Supplementary Information, section 5e). The central cell is triggered at time $t = 0$, and cascades are computed subsequently (Fig. 4f–h). At low densities (regime I, around 1 mm^{-2}), neighbours cannot be reached sufficiently and the signal rapidly dies out. At high densities (regime II,

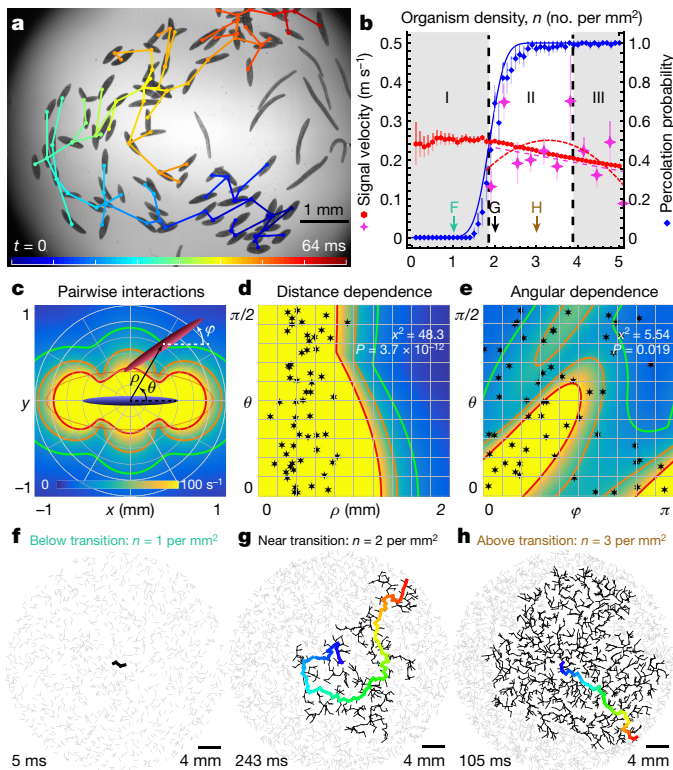


Fig. 4 | Collective hydrodynamic communication. **a**, Trigger wave propagating through a colony. The connecting lines and colours indicate which organisms triggered which other organisms. One experiment with $n = 97$ organisms is shown, out of $n = 41$ experiments. **b**, Phase diagram. Percolation probability ($P(N)$) in simulations (blue diamonds) and theoretical prediction (blue line). Wave velocities ($v_w(N)$) are superimposed, in simulations (red) and experiments (pink stars). The vertical error bars correspond to 2 s.e.m. $n = 97$ organisms. **c**, Pairwise interactions between transmitter A (blue) and receiver B (purple). Background colours show the generated strain rate (equation (1)). The green, orange and red contours correspond to $\dot{\gamma} = 25 \text{ s}^{-1}$, 50 s^{-1} and 100 s^{-1} , respectively. The red contour represents the sensing threshold; that is, the region of influence (which is also approximated by the dashed-red ellipse). **d**, Distance dependence of pairwise interactions. The strain rate on the body of the receiver B is shown for relative positions (ρ, θ), maximizing over all orientations ϕ . Stars are corresponding experimental observations, tested with χ^2 statistics, $n = 57$ experiments (Supplementary Information, section 5c). **e**, Angular dependence, for relative orientations (ϕ, θ) with constant $\rho = 1 \text{ mm}$. **f–h**, Simulations of trigger waves in colonies below, near and above N_c . Grey ellipses are non-triggered organisms. Black lines show the triggered connectivity graph. The first percolating path to the colony edge is shown with colours scaled to the percolation time (bottom left corners).

around 3 mm^{-2}), signals propagate radially outwards and reach the colony edge in large numbers. In between these densities (near the critical density $N_c^{\text{sim}} = 1.970 \pm 0.087 \text{ mm}^{-2}$), the signal does not travel radially but in fractals, similar to lightning-discharge patterns. Here, the probability for a signal to reach the colony edge ($P(N)$) transitions rapidly from zero to one (Fig. 4b). A small change in density therefore has a large effect on the communication potential near criticality (Supplementary Video 9).

This phase transition is understood in terms of percolation theory²⁵. The percolation threshold is estimated analytically as $N_c^{\text{th}} = 1.88 \pm 0.08 \text{ mm}^{-2}$ (Supplementary Information, section 5f). Hence, this theory is in good agreement with our simulations, and with our experiments, in which signals are only sustained above $N_c^{\text{exp}} = 1.91 \pm 0.44 \text{ mm}^{-2}$ (Fig. 4b). The theory also predicts a lower percolation threshold for cells with larger aspect ratios, which again highlights the slender body of *Spirostomum*. Moreover, we find that the communication potential is enhanced for organisms that swim near

water–air interfaces, because these reflect flows (see Supplementary Information, section 5g).

Organism densities that are too high (regime III, around 5 mm^{-2}) might be disadvantageous in terms of sharing food reserves. Swimming and contractions also require more energy in a dense suspension, because the Einstein viscosity increases. Moreover, our simulations show that the wave velocity ($v_w(N)$) reduces with cell density (Fig. 4b, red hexagons); the experiments show the same trend (Fig. 4b, pink stars), albeit with more biological variability. This effect is explained by the fact that the signal is delayed when every organism (per unit area) requires time to perceive and respond (Supplementary Video 10). Consequently, organisms might thrive best near criticality (just above N_c) when optimizing for resources and conductivity.

Hydrodynamic communication could be advantageous for organizing cellular communities, either for defence against large predators (by synchronization of toxin discharge)²⁷, for immobilizing large prey³² or for collective nutrient mixing³, which can be enhanced by a passing hydrodynamic trigger wave (Extended Data Fig. 9, Supplementary Information, section 5h, Supplementary Video 11). As multiple cells contract successively in a colony, particles are subjected to a random walk, with final displacements of over 50% of the cell size—five times more than the inertial mixing of individual cells. Asymmetric contraction and relaxation could further increase this when non-reciprocity is enhanced by higher-order flow contributions.

Beyond immediate survival benefits, hydrodynamic communication could also regulate long-term behaviour as a function of organism density. Signalling pathways could be initiated above a hydrodynamic signal threshold, analogous to bacterial autoinducers that initiate virulence or the formation of biofilms. Particular aspects of this decision-making process may, therefore, be compared with another percolating process—quorum sensing¹⁶—when interpreted as phenotype change that is controlled by cell density (Supplementary Information, section 5i). The *Spirostomum* transcriptome has only recently been sequenced³³ and not much is known about its intercellular pathways; however, long-term habituation to touch already suggests phenotype change³⁴. As in quorum sensing, the judgement of an individual cell to respond to a stimulus must be gauged carefully—not only for energy efficiency but also because the extreme forces generated in repeated contractions can potentially damage cells. The trade-off between individual risk and collective advantages should therefore optimize the overall biofunctionality of the cells.

The presented percolation theory can naturally be extended to three-dimensional organism colonies by using ellipsoids of revolution. However, on a more fundamental level, we expect hydrodynamic trigger waves to be part of the directed percolation universality class²⁶. Directional symmetry breaking—similar to following one-way streets in a maze—is also observed here. This is important for understanding the fractal nature of cellular connectivity near the critical point, with corresponding critical exponents and properties. Pursuing this could represent a new avenue for future research in biological critical phenomena.

Long-ranged hydrodynamic interactions mediate collective motion in many living fluids^{7–11}. To our knowledge, hydrodynamic trigger waves have not been reported in other systems, but similar rapid contractions feature in many other cells—including the model ciliates *Vorticella*¹ and *Stentor*⁵—which in fact operate at low Reynolds numbers. Many organisms beyond protists both generate and sense flows—from bacteria to fish^{2–7,12–19}—and it would be interesting to uncover what function this signalling pathway might serve in different ecosystems, as well as the limitations that it must overcome. This opens scope for questions regarding how broadly hydrodynamic trigger waves could contribute to collective behaviour^{8–11} and, more generally, to the science of active and adaptive materials.

Reporting summary

Further information on research design is available in the Nature Research Reporting Summary linked to this paper.

Data availability

The data that support the plots within this paper and other findings of this study are available from the corresponding authors upon request.

Code availability

The computer codes used in this paper are available from the corresponding authors upon request.

Online content

Any methods, additional references, Nature Research reporting summaries, source data, extended data, supplementary information, acknowledgements, peer review information; details of author contributions and competing interests are available at <https://doi.org/10.1038/s41586-019-1387-9>.

Received: 25 September 2018; Accepted: 18 June 2019;

Published online 10 July 2019.

- Weis-Fogh, T. & Amos, W. B. Evidence for a new mechanism of cell motility. *Nature* **236**, 301–304 (1972).
- Mahadevan, L. & Matsudaira, P. Motility powered by supramolecular springs and ratchets. *Science* **288**, 95–99 (2000).
- Ryu, S., Pepper, R., Nagai, M. & France, D. *Vorticella*: a protozoan for bio-inspired engineering. *Micromachines* **8**, 4 (2016).
- Ilton, M. et al. The principles of cascading power limits in small, fast biological and engineered systems. *Science* **360**, eaao1082 (2018).
- Marshall, W. F. Origins of cellular geometry. *BMC Biol.* **9**, 57 (2011).
- Purcell, E. M. Life at low Reynolds number. *Am. J. Phys.* **45**, 3 (1977).
- Lauga, E. & Powers, T. R. The hydrodynamics of swimming microorganisms. *Rep. Prog. Phys.* **72**, 096601 (2009).
- Koch, D. L. & Subramanian, G. Collective hydrodynamics of swimming microorganisms: living fluids. *Annu. Rev. Fluid Mech.* **43**, 637–659 (2011).
- Marchetti, M. et al. Hydrodynamics of soft active matter. *Rev. Mod. Phys.* **85**, 1143 (2013).
- Elgeti, J., Winkler, R. G. & Gompper, G. Physics of microswimmers—single particle motion and collective behavior: a review. *Rep. Prog. Phys.* **78**, 056601 (2015).
- Bechinger, C. et al. Active particles in complex and crowded environments. *Rev. Mod. Phys.* **88**, 045006 (2016).
- Winkler, R. G. Low Reynolds number hydrodynamics and mesoscale simulations. *Eur. Phys. J. Spec. Top.* **225**, 2079–2097 (2016).
- Mathijssen, A. J. T. M., Doostmohammadi, A., Yeomans, J. M. & Shendruk, T. N. Hydrodynamics of micro-swimmers in films. *Fluid Mech.* **806**, 35–70 (2016).
- Latz, M. I. et al. Bioluminescent response of individual dinoflagellate cells to hydrodynamic stress measured with millisecond resolution in a microfluidic device. *J. Exp. Biol.* **211**, 2865–2875 (2008).
- Kjørboe, T., Andersen, A., Langlois, V. J., Jakobsen, H. H. & Bohr, T. Mechanisms and feasibility of prey capture in ambush-feeding zooplankton. *Proc. Natl Acad. Sci. USA* **106**, 12394–12399 (2009).
- Kim, M. K., Ingremeau, F., Zhao, A., Bassler, B. L. & Stone, H. A. Local and global consequences of flow on bacterial quorum sensing. *Nat. Microbiol.* **1**, 15005 (2016).
- Rodesney, C. A. et al. Mechanosensing of shear by *Pseudomonas aeruginosa* leads to increased levels of the cyclic-di-GMP signal initiating biofilm development. *Proc. Natl Acad. Sci. USA* **114**, 5906–5911 (2017).
- Ohmura, T. et al. Simple mechanosense and response of cilia motion reveal the intrinsic habits of ciliates. *Proc. Natl Acad. Sci. USA* **115**, 3231–3236 (2018).
- Wan, K. Y. & Goldstein, R. E. Time irreversibility and criticality in the motility of a flagellate microorganism. *Phys. Rev. Lett.* **121**, 058103 (2018).
- Tyson, J. J. & Keener, J. P. Singular perturbation theory of traveling waves in excitable media (a review). *Physica D* **32**, 327–361 (1988).
- Prindle, A. et al. Ion channels enable electrical communication in bacterial communities. *Nature* **527**, 59–63 (2015).
- Gelens, L., Anderson, G. A. & Ferrell, J. E. Jr. Spatial trigger waves: positive feedback gets you a long way. *Mol. Biol. Cell* **25**, 3486–3493 (2014).
- Hawkes, R. B. & Holberton, D. V. Myonemal contraction of *Spirostomum*. I. Kinetics of contraction and relaxation. *J. Cell. Physiol.* **84**, 225–235 (1974).
- Phillips, R., Kondev, J., Theriot, J. & Garcia, H. *Physical Biology of the Cell* (Garland Science, 2012).
- Xia, W. & Thorpe, M. F. Percolation properties of random ellipses. *Phys. Rev. A Gen. Phys.* **38**, 2650–2656 (1988).
- Takeuchi, K. A., Kuroda, M., Chaté, H. & Sano, M. Directed percolation criticality in turbulent liquid crystals. *Phys. Rev. Lett.* **99**, 234503 (2007).
- Buonanno, F., Guella, G., Strim, C. & Ortenzi, C. Chemical defence by mono-perenyl hydroquinone in a freshwater ciliate, *Spirostomum ambiguum*. *Hydrobiologia* **684**, 97–107 (2012).
- Verhot-Lubicz, J. & Goldstein, R. E. Cytoplasmic streaming enables the distribution of molecules and vesicles in large plant cells. *Protoplasma* **240**, 99–107 (2010).
- Nüchter, T., Benoit, M., Engel, U., Ozbek, S. & Holstein, T. W. Nanosecond-scale kinetics of nematocyst discharge. *Curr. Biol.* **16**, R316–R318 (2006).
- Hawking, S. W. *A Brief History of Time* (Bantam Books, 1988).
- Cortez, R., Fauci, L. & Medovikov, A. The method of regularized Stokeslets in three dimensions: analysis, validation, and application to helical swimming. *Phys. Fluids* **17**, 031504 (2005).
- K. Hausmann, Food acquisition, food ingestion and food digestion by protists. *Jpn. J. Protozool.* **35**, 85–95 (2002).
- Hines, H. N., Onsbring, H., Ettema, T. J. G. & Esteban, G. F. Molecular investigation of the ciliate *Spirostomum semivirescens*, with first transcriptome and new geographical records. *Protist* **169**, 875–886 (2018).
- Hamilton, T. C., Thompson, J. M. & Eisenstein, E. M. Quantitative analysis of ciliary and contractile responses during habituation training in *Spirostomum ambiguum*. *Behav. Biol.* **12**, 393–407 (1974).

Publisher's note: Springer Nature remains neutral with regard to jurisdictional claims in published maps and institutional affiliations.

© The Author(s), under exclusive licence to Springer Nature Limited 2019

Acknowledgements We thank S. Coyle and D. Krishnamurthy and all members of the Prakash Laboratory for discussions. A.J.T.M.M. acknowledges funding from the Human Frontier Science Program (Fellowship LT001670/2017). This work was supported by NSF CCC grant (DBI-1548297) (M.P.), US Army Research Office grant (W911NF-15-1-0358) (M.P.), CZI BioHub Investigator Program (M.P.), the Howard Hughes Medical Institute (M.P.) and NSF grant (award number 1817334) (M.S.B.). We thank M. Gruber for the scientific illustration of *S. ambiguus* shown in Fig. 1a.

Author contributions A.J.T.M.M., M.S.B. and M.P. designed the research, A.J.T.M.M., M.S.B. and J.C. performed the experiments, A.J.T.M.M. analysed the data, A.J.T.M.M. carried out the simulations and theory, A.J.T.M.M., M.S.B., J.C. and M.P. wrote the manuscript.

Competing interests The authors declare no competing interests.

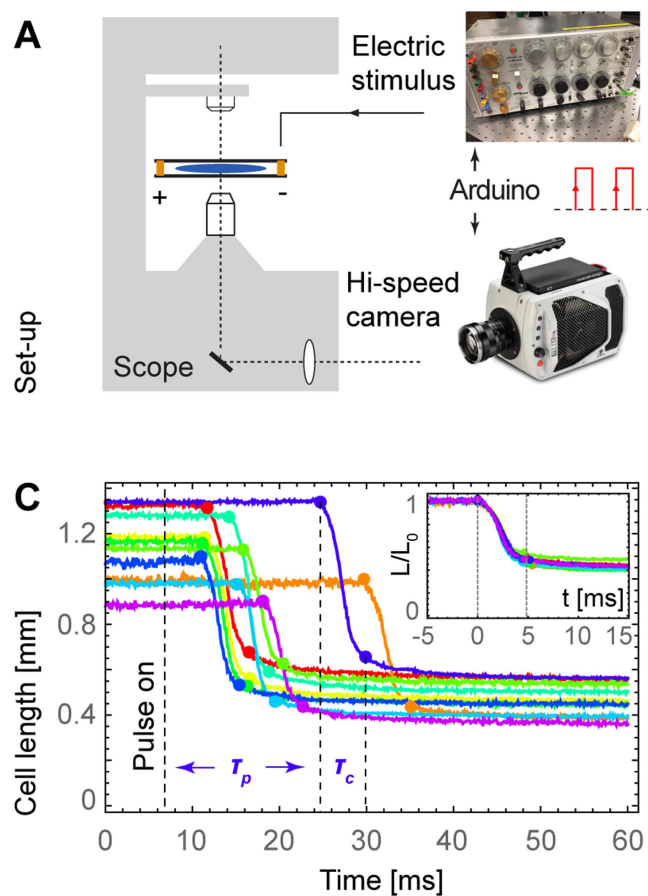
Additional information

Supplementary information is available for this paper at <https://doi.org/10.1038/s41586-019-1387-9>.

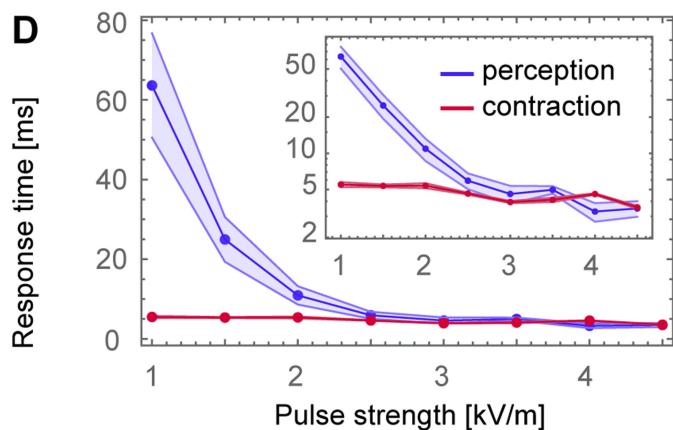
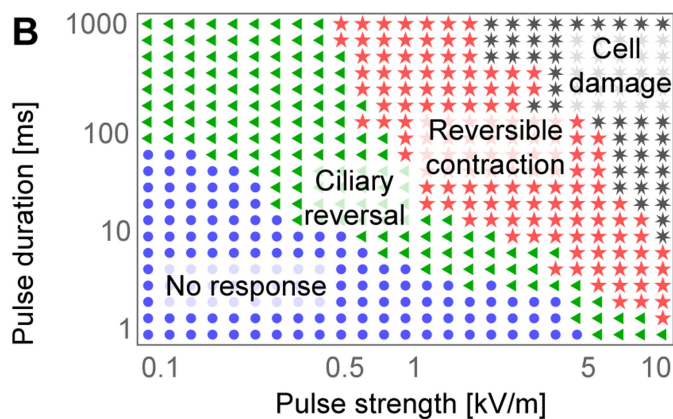
Correspondence and requests for materials should be addressed to M.S.B. or M.P.

Peer review information *Nature* thanks Shiladitya Banerjee, Gerhard Gompper, Pavel Tomancak and the other anonymous reviewer(s) for their contribution to the peer review of this work.

Reprints and permissions information is available at <http://www.nature.com/reprints>.

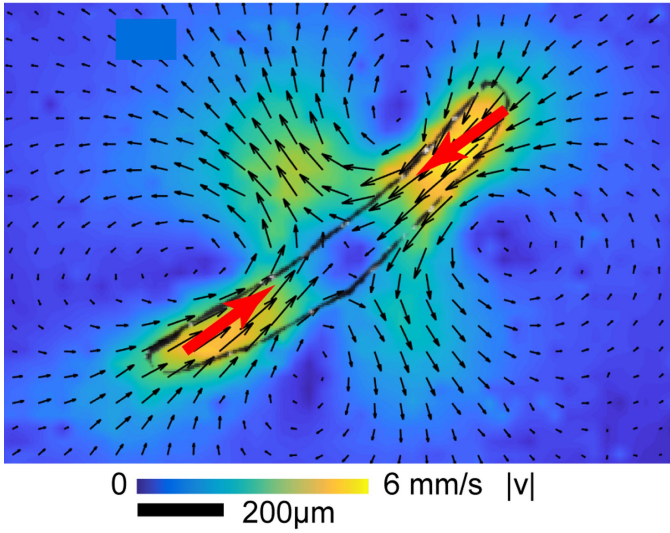


Extended Data Fig. 1 | Measurement of electrically stimulated *Spirostomum* contraction dynamics. **a**, Diagram of experimental setup. **b**, Phase diagram of organism response to electric signals. The median behaviour of about 20 organisms is shown for each data point; this is repeated in $n = 20 \times 25$ independent experiments with new organisms, for different pulse strengths and duration. **c**, Typical kinematics of organism length after stimulation at $E = 1.5 \text{ kV m}^{-1}$ and $\tau_E = 100 \text{ ms}$. Inset, collapse

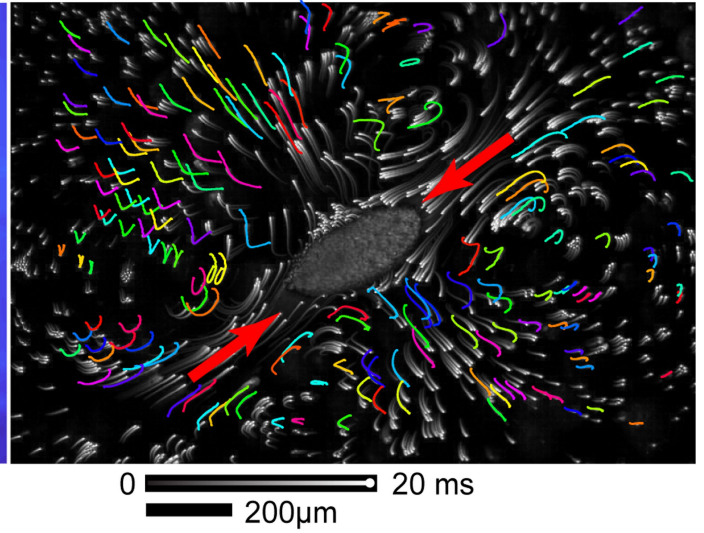


of kinematics, when normalizing the cell length and lining up the onsets of contraction at $t = 0$. **d**, Perception and contraction time against stimulus intensity, with $\tau_E = 100 \text{ ms}$. Points show the mean of an ensemble of about 20 independent organisms for each pulse strength, and shaded regions are error bars of 95% confidence level. The inset shows the same data on a log scale.

PIV experiment

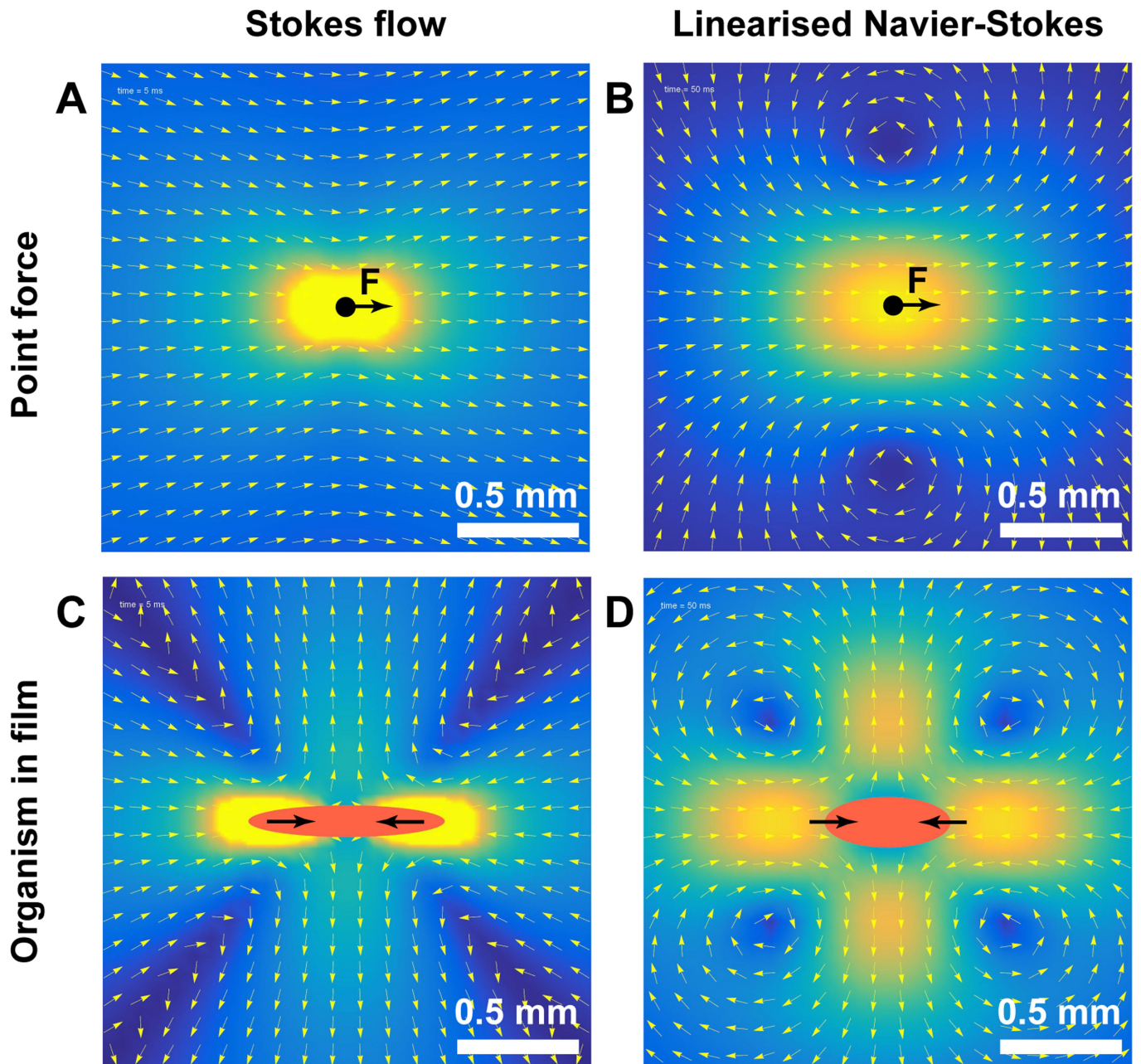


PTV & FlowTrace experiment



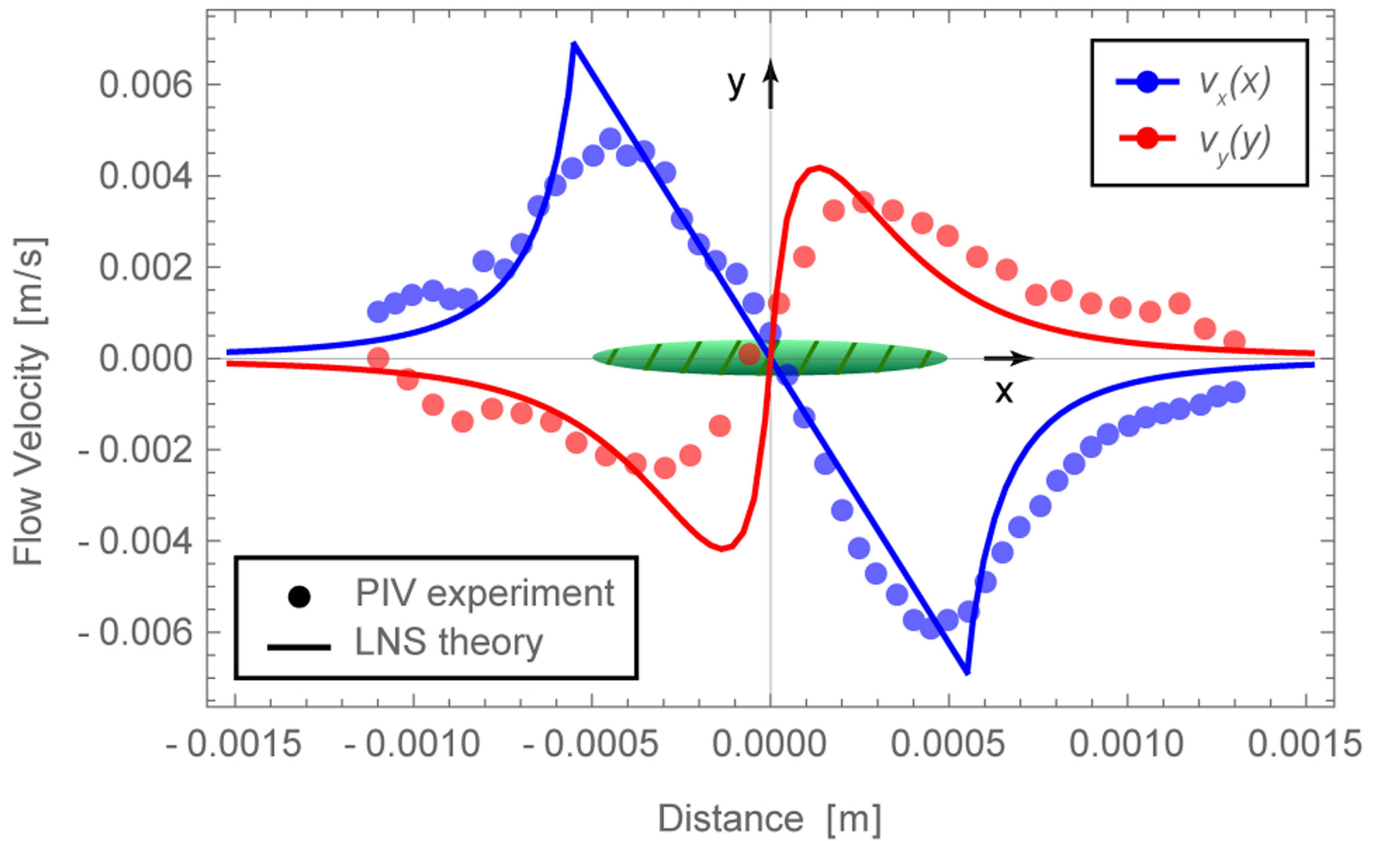
Extended Data Fig. 2 | Experimental data of the generation of flow during contractions. Data are the same as those presented in Fig. 2c, d, but without the theory data superimposed. The red arrows that denote the long axis of the body are kept for reference. $n = 46$ experiments. **a**, PIV measurements of the flow averaged for 40 ms after the onset of

contraction. **b**, Experimental tracer dynamics. White lines are obtained from superposing image frames with FlowTrace software, and the coloured lines are digital PTV particle trajectories obtained with TrackMate software.



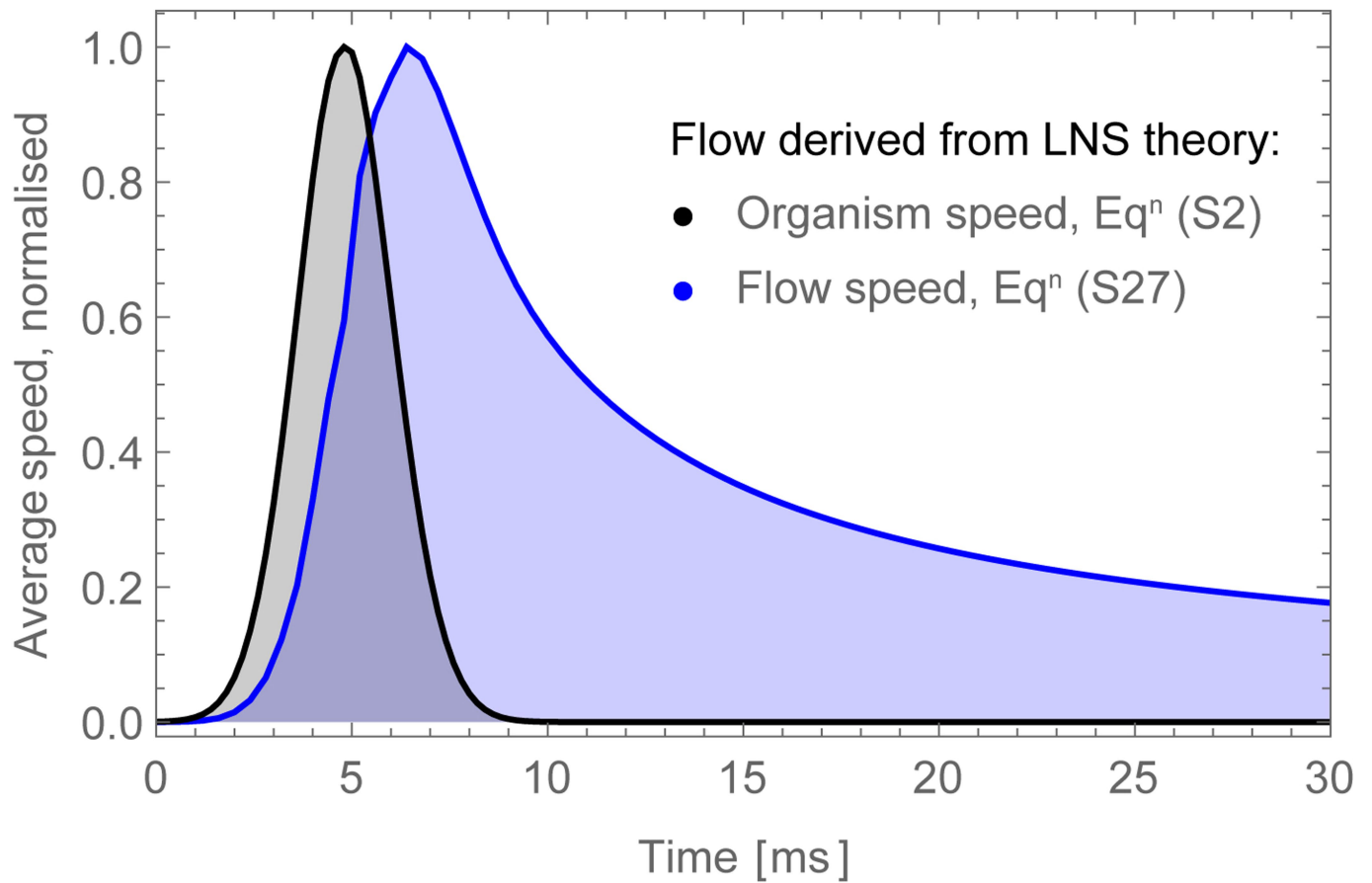
Extended Data Fig. 3 | Comparison of Stokes flow and LNS flow. Stokes flow, $Re_T \ll 1$; linearized Navier Stokes flow, $Re_T \approx 50$. **a**, Flow due to a point force (Stokeslet solution) (Supplementary equation 10). **b**, LNS tensor solution (Supplementary equation 16). **c**, **d**, Contraction flow in a liquid film (Supplementary equation 27); for high ($1,000\times$ water) (c) and low (water) (d) viscosities, with $m = \pm 100$ image reflections and

$k = \pm 5$ grid points on the elongated body. In this figure, τ_c is kept constant at 5 ms for comparison of the high- and low-viscosity cases. The Stokes solution has open stream lines, but the LNS solution features vortices that spread out over time. Colours show flow magnitude and arrows are stream lines.



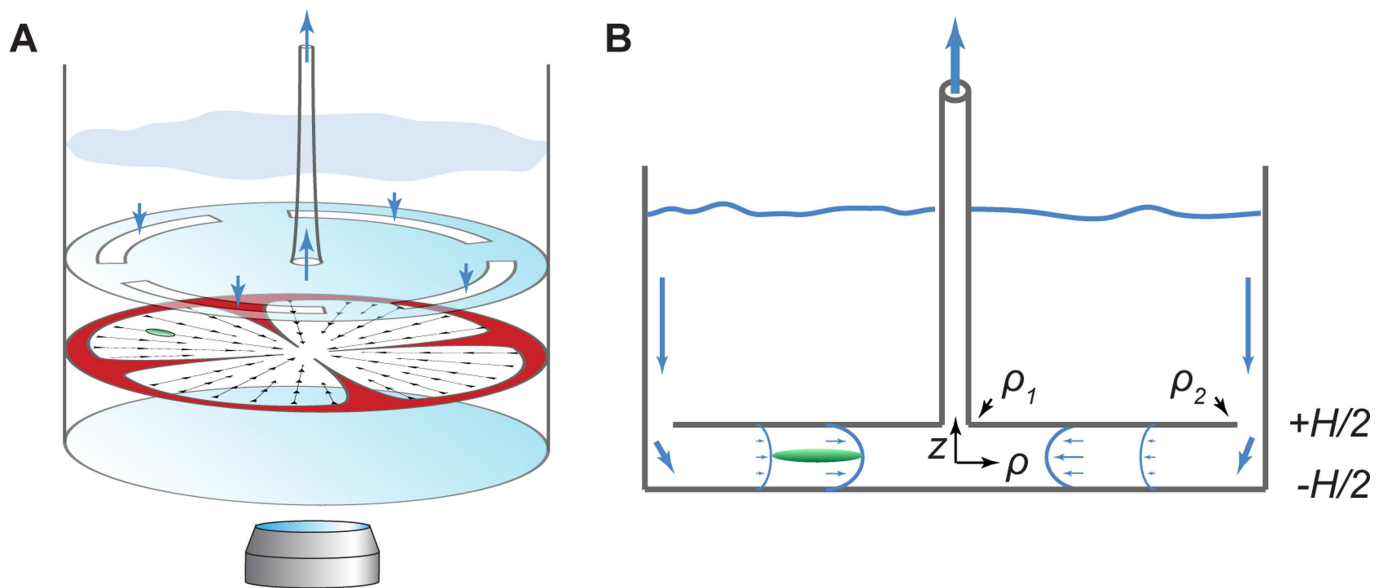
Extended Data Fig. 4 | Comparison of experimental and theoretical flows induced by a cell contracting in a liquid film. Flow velocities are shown, as a function of distance from the organism. Results were obtained experimentally (PIV) and theoretically (LNS model; Supplementary equation 27), and both are averaged for the 40 ms after the onset of

contraction. These are the same data as are shown in Fig. 2c, shown differently to aid quantitative comparison. Blue and red colours indicate flows in the longitudinal and transverse directions, respectively, of the elongated cell, which is shown in green for reference. Points indicate experimental data and lines indicate the model. $n = 46$ experiments.



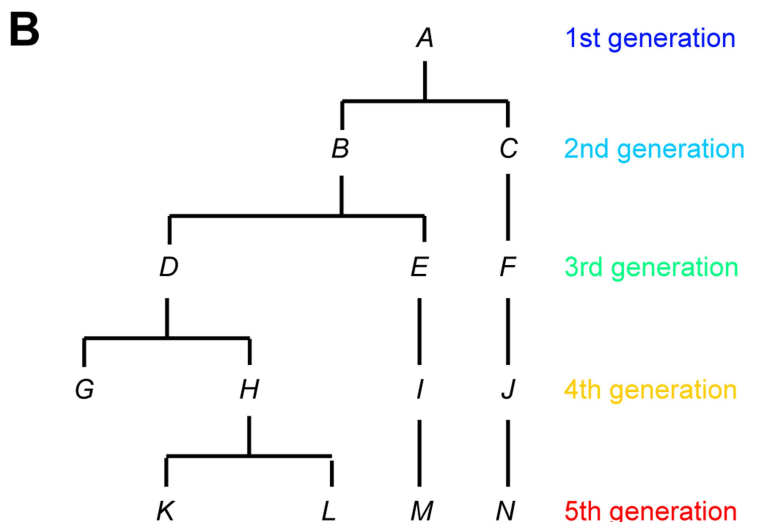
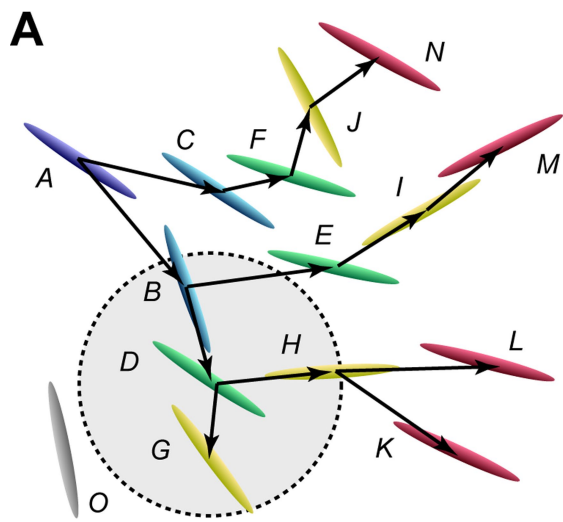
Extended Data Fig. 5 | Dissipation of the spatially averaged flow velocity over time. Results are obtained from the LNS model (Supplementary equation 27) for a low viscosity medium (water, $\nu = 1 \text{ mm}^2 \text{ s}^{-1}$). The average is taken over all spatial points x ,

$y \in [-1, 1] \text{ mm}$, at the centre of the liquid film, $z = 0$ (the same data as are presented in Supplementary Video 5). Speeds are normalized with respect to their maximum. These simulation data may be compared directly with the experimental data in Fig. 2e.



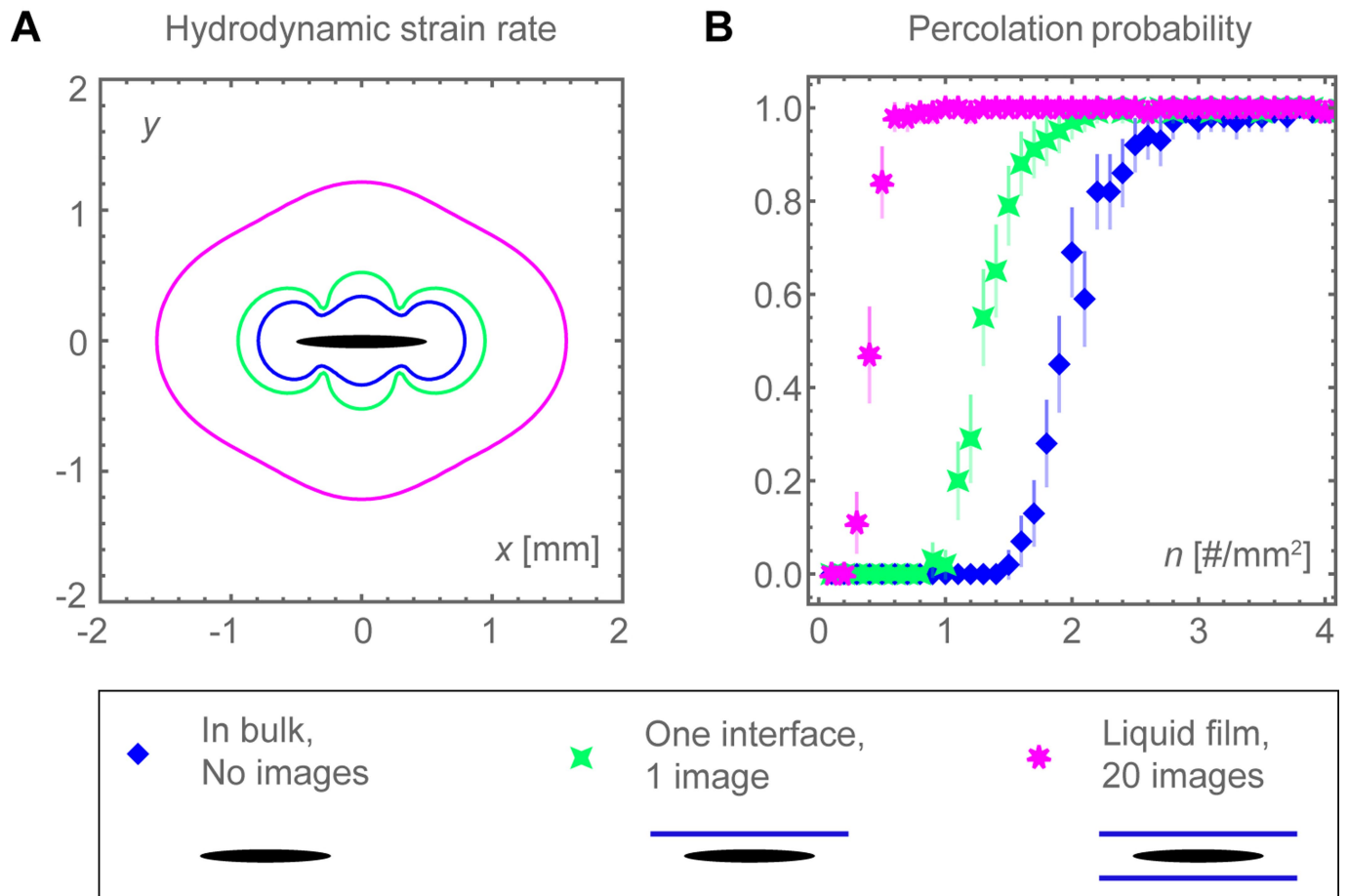
Extended Data Fig. 6 | Diagram of the high-throughput device developed for measuring the rheosensitivity of cells. The device is not shown to scale. Liquid with suspended organisms is held in a cylindrical container, with a narrow flow chamber in the bottom compartment. Liquid is drawn into the chamber on the sides and pumped out from a central

tube. This creates an axisymmetric Jeffery–Hamel flow (Supplementary equation 29). **a**, Three-dimensional diagram of the experimental setup. **b**, Side view and schematic of flow profile. The organism (green) is stretched because the anterior flow is stronger than the posterior flow (Supplementary equation 33).



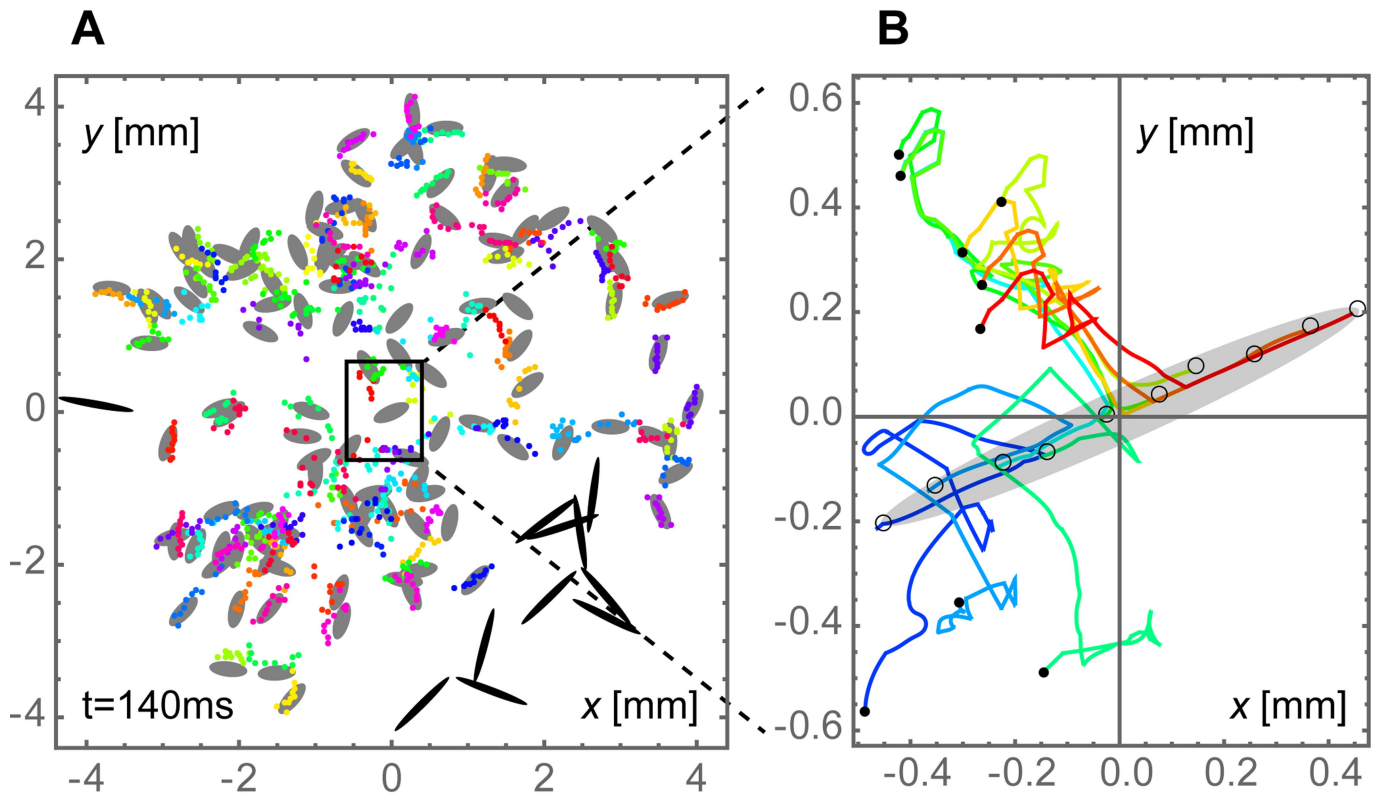
Extended Data Fig. 7 | Collective hydrodynamic signalling. **a**, Example of a configuration of organisms A–O. The first cell to contract is A (blue), and the last are K, L, M and N (red). Organism O is not triggered (grey).

The circle is used to compute the organism density around cell D (green). **b**, Connectivity graph of the same configuration as shown in **a**.



Extended Data Fig. 8 | Effect of boundary conditions on the percolation threshold. Three geometries are considered: (1) organisms in bulk, without confining surfaces (blue). This situation is presented in the main text. (2) Organisms at $z = 0$ near a liquid–air interface at $z = 50 \mu\text{m}$ (green). Here, one reflecting image system is used. (3) Organisms in a liquid film, between liquid–air interfaces at $z = \pm 50 \mu\text{m}$, for which a series of reflecting image systems is used (magenta). In all three cases, the cells are located at $z = 0$ and oriented parallel to the x - y plane, for comparison.

a, Contours of the critical strain rate $\dot{\gamma}_c = 100 \text{ s}^{-1}$ for each of the three geometries (compare with Fig. 4c). This region of influence is largest in a film. **b**, Simulated percolation probability versus organism density for each geometry (compare with Fig. 4b). The percolation threshold is lowest in the film. Centre values show the mean of an ensemble of $n = 100$ independent simulations, each with about 10^3 cells, and the error bars indicate two s.e.m.



Extended Data Fig. 9 | Mixing of toxins during a hydrodynamic trigger wave. Simulated for $n = 123$ organisms in an approximately 1-cm-diameter colony, at a cell density of $n = 2.5$ organisms per mm^2 . **a**, Final frame of Supplementary Video 11 after the trigger wave has passed. Coloured points indicate toxin particles released by different organisms in the colony. Grey organisms (ellipses) are triggered; black cells are not triggered. **b**, Trajectories of ten simulated toxin particles released by a

single organism during a hydrodynamic trigger wave. Colours distinguish tracks of the different particles, black circles are the initial positions of the particles and the black points are the final positions of the particles. At the first contraction, the particles are mostly pulled inwards; with subsequent contractions of other cells, the particles follow a random walk and spread out.

Reporting Summary

Nature Research wishes to improve the reproducibility of the work that we publish. This form provides structure for consistency and transparency in reporting. For further information on Nature Research policies, see [Authors & Referees](#) and the [Editorial Policy Checklist](#).

Statistics

For all statistical analyses, confirm that the following items are present in the figure legend, table legend, main text, or Methods section.

n/a Confirmed

- The exact sample size (n) for each experimental group/condition, given as a discrete number and unit of measurement
- A statement on whether measurements were taken from distinct samples or whether the same sample was measured repeatedly
- The statistical test(s) used AND whether they are one- or two-sided
Only common tests should be described solely by name; describe more complex techniques in the Methods section.
- A description of all covariates tested
- A description of any assumptions or corrections, such as tests of normality and adjustment for multiple comparisons
- A full description of the statistical parameters including central tendency (e.g. means) or other basic estimates (e.g. regression coefficient) AND variation (e.g. standard deviation) or associated estimates of uncertainty (e.g. confidence intervals)
- For null hypothesis testing, the test statistic (e.g. F , t , r) with confidence intervals, effect sizes, degrees of freedom and P value noted
Give P values as exact values whenever suitable.
- For Bayesian analysis, information on the choice of priors and Markov chain Monte Carlo settings
- For hierarchical and complex designs, identification of the appropriate level for tests and full reporting of outcomes
- Estimates of effect sizes (e.g. Cohen's d , Pearson's r), indicating how they were calculated

Our web collection on [statistics for biologists](#) contains articles on many of the points above.

Software and code

Policy information about [availability of computer code](#)

Data collection

Imaging tools including high-speed camera (Phantom v2012) was used with Imaging software PCC (2.1).

Data analysis

Tracer trajectories and velocities were obtained with "TrackMate" PTV software (Tinevez, J.-Y. et al. Trackmate: An open and extensible platform for single-particle tracking. *Methods* 115, 80–90 (2017). The description of all the other data analysis techniques is provided in the paper. FlowTrace (https://github.com/williamgilpin/flowtrace_python) used for visualization. Matlab 2018 used for analysis.

For manuscripts utilizing custom algorithms or software that are central to the research but not yet described in published literature, software must be made available to editors/reviewers. We strongly encourage code deposition in a community repository (e.g. GitHub). See the Nature Research [guidelines for submitting code & software](#) for further information.

Data

Policy information about [availability of data](#)

All manuscripts must include a [data availability statement](#). This statement should provide the following information, where applicable:

- Accession codes, unique identifiers, or web links for publicly available datasets
- A list of figures that have associated raw data
- A description of any restrictions on data availability

No restrictions exists on data availability. The key datasets for all the plots and simulations including videos are included in the submission.

Field-specific reporting

Please select the one below that is the best fit for your research. If you are not sure, read the appropriate sections before making your selection.

Life sciences Behavioural & social sciences Ecological, evolutionary & environmental sciences

For a reference copy of the document with all sections, see nature.com/documents/nr-reporting-summary-flat.pdf

Life sciences study design

All studies must disclose on these points even when the disclosure is negative.

Sample size

Sample size of number of cells used and number of times experiments are repeated for each figures is provided in main figures and supplementary figures. The associated statistical tests are provided in the supplementary materials. Details: Fig 1B: This SEM experiment was independently repeated $N_e = 21$ times with different organisms, giving similar results.
 Fig 1C: This contraction kinematics experiment was independently repeated $N_e = 48$ times with different organisms, giving similar results. Note that these are spontaneous contractions that were not triggered electrically.
 Fig 1E: This contraction kinematics experiment was independently repeated $N_e = 216$ times with different organisms, at 8 different pulse strengths. See §IIB for more details.
 Fig 2C-D: This particle image velocimetry (PIV) experiment was independently repeated $N_e = 46$ times with different organisms, with tracer particles of different diameters, $D = 0.75, 1, 2, 6\mu\text{m}$, all showing similar results. See §III A for more details.
 Fig 2E: This particle tracking velocimetry (PTV) experiment uses an ensemble of $N_t = 171$ tracer particles to determine the averaged flow velocity over time. See §III A for more details. The low-viscosity were repeated $N_e = 46$ times with similar results, and $N_e = 17$ for the high-viscosity control experiments.
 Fig 2F: This mixing simulation uses an ensemble of $N_t = 500$ tracer particles, and was repeated independently for the high and low viscosity cases. See §III E for more details. Fig 3B-E: This rheosensing experiment comprised of $N_o = 115$ different organisms. See §IV A for more details. This experiment was independently repeated $N_e = 17$ times with similar results.
 Fig 3E: Box-whisker chart definition: Whiskers show the upper and lower fences (outliers), the box edges show the 25% and 75% quantiles, and the middle line is the median.
 Fig 4A: Shown is one hydrodynamic trigger wave experiment with $N_o = 97$ organisms. This hydrodynamic trigger wave experiment was independently repeated $N_e = 41$ times giving similar results. See §VB for more details.
 Fig 4B: This phase diagram shows simulations (blue) for an ensemble of $N_e = 100$ independent colonies, each with $N_o \sim 103$ organisms depending on the density [see §V E]. The trigger wave velocity experiment (pink) used $N_o = 97$ organisms, and was repeated $N_e = 41$ times with similar results.
 Fig 4D,E: This pairwise contraction experiment was independently repeated $N_e = 57$ times with different organisms. See §V C for more details.
 Fig S1B: Shown is the median behaviour of $N_o > 20$ organisms for each data point, which is repeated in $N_e = 20 \times 25$ independent experiments with new organisms for different pulse strengths and duration.
 Fig S1C,D: This contraction kinematics experiment was independently repeated with $N_e = 28, 38, 47, 26, 30, 18, 19, 10$ organisms at applied voltages 10, 15, 20, 25, 30, 35, 40, 45V, respectively. See §IIB for more details.
 Fig S2,4,5: These flow measurement experiments were independently repeated $N_e = 46$ times with different organisms, giving similar results.
 Fig S8: These hydrodynamic trigger wave simulations were repeated for an ensemble of $N_e = 100$ independent colonies, each with $N_o \sim 103$ organisms depending on the density [see §V G].

Data exclusions

No data has been excluded.

Replication

Extensive efforts were taken throughout data collection process to ensure replication and reproducibility. The list above on sample size goes through step by step on choices made on samples. With large sample sizes and no data excluded; replication is documented in figures plotted already. Furthermore, we replicated experiments at two different locations in two labs - one in primary lab at Stanford and a few experiments were also recreated and replicated in a former postdoc's lab in Georgia Tech.

Randomization

Single cells were randomly picked from cultures and randomly chosen for imaging. For studies involving length related correlations, data was collected on a randomly sampled group of cells and sorted as a function of cell length.

Blinding

Blinding was not relevant for our study since no a-prior grouping was done on cells used in the experiments.

Reporting for specific materials, systems and methods

We require information from authors about some types of materials, experimental systems and methods used in many studies. Here, indicate whether each material, system or method listed is relevant to your study. If you are not sure if a list item applies to your research, read the appropriate section before selecting a response.

Materials & experimental systems

n/a	Included in the study
<input checked="" type="checkbox"/>	<input type="checkbox"/> Antibodies
<input checked="" type="checkbox"/>	<input type="checkbox"/> Eukaryotic cell lines
<input checked="" type="checkbox"/>	<input type="checkbox"/> Palaeontology
<input type="checkbox"/>	<input checked="" type="checkbox"/> Animals and other organisms
<input checked="" type="checkbox"/>	<input type="checkbox"/> Human research participants
<input checked="" type="checkbox"/>	<input type="checkbox"/> Clinical data

Methods

n/a	Included in the study
<input checked="" type="checkbox"/>	<input type="checkbox"/> ChIP-seq
<input checked="" type="checkbox"/>	<input type="checkbox"/> Flow cytometry
<input checked="" type="checkbox"/>	<input type="checkbox"/> MRI-based neuroimaging

Animals and other organisms

Policy information about [studies involving animals](#); [ARRIVE guidelines](#) recommended for reporting animal research

Laboratory animals

The study involves single cell ciliates Spirostomum ambiguum; which were obtained from Carolina Biological and cultured in the lab.

Wild animals

The study did not involve wild animals.

Field-collected samples

The study did not involve field collected samples.

Ethics oversight

The study did not require any ethics approval or guidance.

Note that full information on the approval of the study protocol must also be provided in the manuscript.